UC San Diego
UC San Diego Previously Published Works

Title

Self-Sustained Robots Based on Functionally Graded Elastomeric Actuators Carrying up to 22 Times Their Body Weight

Permalink

https://escholarship.org/uc/item/9h8410xp

Journal

Advanced Intelligent Systems, 5(4)

ISSN

2640-4567

Authors

Zhai, Yichen

Ng, Tse Nga

Publication Date

2023-04-01

DOI

10.1002/aisy.202100085

Peer reviewed

RESEARCH ARTICLE

ADVANCED
INTELLIGENT
SYSTEMS
Open Access

www.advintellsyst.com

Self-Sustained Robots Based on Functionally Graded Elastomeric Actuators Carrying up to 22 Times Their Body Weight

Yichen Zhai and Tse Nga Ng*

A biomimetic strategy of combining soft actuators with an exoskeleton is applied to create untethered, self-sustained robots with high load capacity, applicable for transportation in unsupervised environments. The soft actuation components are based on liquid crystal elastomers formed into functionally graded structures by extrusion printing, which enables a high free strain of 45.5%. The robot design includes a self-sustained oscillation mechanism incorporating a novel, highly elastic spring for energy storage and impulse release. The arthropod-inspired exoskeleton structures are printed from polycarbonate with high strength to increase the load-carrying capacity, or to increase moving speed by a lever mechanism that amplifies the stepping distance up to eight times. The robot achieves self-sustained locomotion, harvesting constant infrared radiation for continual power. Leveraging the strength of the exoskeleton and the high stress of the actuator, the robot transports a load 22 times its body weight. It is capable of climbing up a slope of 40° and moving up to a quarter of its body length per minute with peripheral lever legs. The robot operation does not require external signaling controls or complex electronics, demonstrating the potential of this battery-free, scalable, environment-powered design with an unlimited range free from tethering constraints.

1. Introduction

Untethered robots that acquire energy from the ambient to produce self-sustained movement can open new avenues for realizing autonomous transporters with unlimited range. Currently many untethered robots rely on batteries[1–4] with limited capacities; others are wirelessly controlled by a nearby magnetic field[5–9] or light stimuli,[10–16] but the robots must stay within the range of controlling signals to be powered. There is emerging research to

Y. Zhai, T. N. Ng
Department of Electrical and Computer Engineering
University of California San Diego
La Jolla, CA 92093, USA
E-mail: tnn046@ucsd.edu

The ORCID identification number(s) for the author(s) of this article can be found under https://doi.org/10.1002/aisy.202100085.

generate sustained motion that does not depend on intermittent switching of external stimuli so that the robots can harness constant environmental energy and convert it to generate locomotion free of distance constraints. Stimuli-responsive polymers such as hydrogels[17,18] and liquid crystal elastomers[12] have been used in designs with oscillatory feedback loops, such as self-shadowing,[18–20] electric powering from tracks,[21] or ratchet[17] mechanisms, to produce bursts of kinetic energy for propulsion. Although these ingenious designs have led to self-sustained movement, the polymer robots are limited in their load-carrying capability. The soft robots are deformed by the load, and so far they can only carry loads within the same order as their own body weights,[1,14,22–26] restricting their applications as transporters.

In this article, a biomimetic strategy of combining soft actuators with an exoskeleton is applied to create self-sustained robots with high load capacity. In the natural world, arthropods like leaf-cutter ants develop exoskeletons that enable them to carry loads exceeding their body weights by hundreds of times.[27] The exoskeleton provides strong supporting structures for the soft muscles to withstand the extra pressure from heavy loads. The actuating muscles are not encumbered by the weight of an internal skeletal system and can apply most of their output forces to lifting external objects. This work used heat-responsive liquid crystal elastomers (LCEs) as actuating components.[28–30] The thermal actuation mechanism of LCEs is advantageous for developing heat-harvesting schemes to mimic another aspect of arthropods, in that cold-blooded insects absorb sunlight and leverage the heat to warm up for activities. Here, we present design principles that harness thermal changes in LCE materials to drive an oscillating ratchet to continually power exoskeleton robots without range limitations and demonstrate an autonomous transporter capable of carrying payloads much heavier than their own weight.

We fabricated the robots by extrusion printing,[31–34] in which the hard components are made of polycarbonate with high strength, and the soft actuators are based on an LCE with properties tuned by the printing parameters. The direct printing process enables the fabrication of functionally graded structures, in particular to engineer new system-level functions beyond the bulk mechanics of component materials. Previous works have adjusted

the shear stress during printing to tailor LCE mesogen alignment[31–33] and demonstrate free-form deformations. However, the power output of LCE actuators is hampered by the long transition time between actuation and relaxation. To accelerate LCE movement, we introduce a novel design of printed LCE springs to store and release energy in cooperation with the LCE actuator. The printed spring offers a tunable elastic modulus, larger tensile breaking strength, and a higher restoring force than polydomain elastomers. This new spring component greatly expands the design space for LCE actuation, so we can realize self-oscillation in LCE systems and facilitate continuous operation similar to engine cycles. In addition to the spring-and-ratchet mechanism, we include a lever amplifier to increase the stepping distance in a robot stride. The robot is characterized on various hill grades, tested for its load-carrying limits, and demonstrates self-sustained locomotion under sunlight, to show the potential of this battery-free, scalable design for environment-powered actuators.

2. Results

2.1. Programming LCE Mechanical Properties by Adjusting Toolpath and Shear Stress

For our bioinspired robot, the artificial muscle is based on an LCE structure with two segments, one being a conventional monodomain actuator and the other functioning as a spring. In the LCE actuator, the liquid crystal mesogens are set in alignment at room temperature. When the actuator slab is heated, the alignment is disrupted by thermal motion. The slab becomes isotropic and contracts in length as shown in **Figure 1**a. The contraction is reversible; when cooled, the LCE recovers to its original shape at room temperature.

A common technique for aligning the mesogens is by applying a shear force on the ink during the extrusion process. Prior works showed that inside a printing nozzle, due to the difference in flow velocities at the center and around the rim, the LCE ink was sheared in a tubular distribution, resulting in better mesogen alignment in the outer shell while the inner core remained isotropic.[31,32] To avoid uneven alignment in a filament, we modified our printing process to reduce the distance between the nozzle tip and the deposition surface, keeping the distance less than half of the inner diameter of the nozzle. As such, the extruded material was squashed by the nozzle edge as shown in Figure 1b. The moving nozzle applied a shear force parallel to the printing direction, and the shear stress generated in the LCE materials was adjusted by tuning the ink flow rate and deposition layer height. The relationships of shear stress as a function of printing parameters were measured as shown in Figure S1, Supporting Information. In general, faster flow rates and thinner layer heights led to a higher shear stress.

The actuators printed under increasing shear stress showed larger free strain (deformation with no load) in Figure 1c. Free strain is defined as $\sigma = (L_0 - L)/L_0$, where L_0 is the original length at room temperature and L is the final length at the actuation temperature. The dependence of free strain on printing shear stress can be empirically fitted to a logarithmic function, indicated by the dashed line in Figure 1c. The function is $\sigma = 0.044 \ln(\tau/\tau_0) + 0.197$, where τ is the shear stress and $\tau_0 = 1$ Pa is a reference value to balance the unit. With our extrusion technique, the actuator reached a maximum free strain of 45.5%, which is higher than the state-of-the-art performance for LCEs.[2,31,32]

The actuator was printed with a toolpath of parallel in-fills and designed to exhibit high contraction force and strain. However, it was limited by a slow cooling process to return to its original length. Thus, we created a spring segment that applied tension on the actuator to accelerate its recovery. There were two requirements for the LCE spring: 1) the spring dimensions should be less affected by temperature compared to the actuator and 2) considering that the spring would be subjected to large stretching strain, it must tolerate high tensile strains before reaching the breaking point and also a high elastic modulus to store and release potential energy. We note that a polydomain LCE, in which mesogens are not aligned, would meet the first condition, but it shows low elastic modulus and high dissipation, resulting in low elastic force and low energy storage efficiency, insufficient for our purpose of cycling the actuator back to its original position. Another option is to look for different elastomers with the desired elasticity, but here we use engineering strategies[31–33,35–40] to tune the mechanical properties and increase the material versatility.

To make a high-performance spring from the LCE, we changed the printing toolpath and directed the mesogen alignment to follow the incline pattern, as shown in Figure 1d. Although the incline direction was the same in each layer, the direction alternated between odd and even layers, with a symmetric incline angle θ. With this metastructure, the dimensional changes in response to heat were suppressed in the spring. When the spring was heated, the tendency for one layer to contract was offset by the pulling forces from the neighboring layers and vice versa, as visualized by the force vector diagram in Figure 1e. The result was that this new spring design decoupled the thermal actuation behavior from being an inherent characteristic in monodomain LCE structures. The printed spring was made less sensitive to heat and showed much lower contraction strain than the actuator, evident in the photographs of Figure 1d, while keeping the advantage of high elasticity in the monodomain LCE. Detailed photographs of the spring metastructure at different temperatures are shown in Figure S1e, Supporting Information.

Figure 1f compares the stress–strain characteristics of an actuator and two different springs with incline angles of 35 and 45°. The x-intercepts (negative values) indicate the free strain values measured at 100 °C. Thermal actuation was reduced with an increasing incline angle in the spring, suppressed to a minimum of 10% strain at $\theta = 45°$. In Figure 1f, the black dots right before abrupt drops in stress denote the breaking stress and strain. The breaking stress of the LCE actuator and that of the springs were similar, in the range of 400 kPa. Yet the actuator broke at low tensile strain (23%) because of its thermally activated contraction, which placed additional countering force to the applied tensile strain. In contrast, the spring did not have this countering force and was able to tolerate more stretching. The springs could be stretched at least three times longer than the actuator before breaking, and this elastic property would be an important characteristic to achieve the oscillatory mechanism for self-sustained locomotion in the following work.
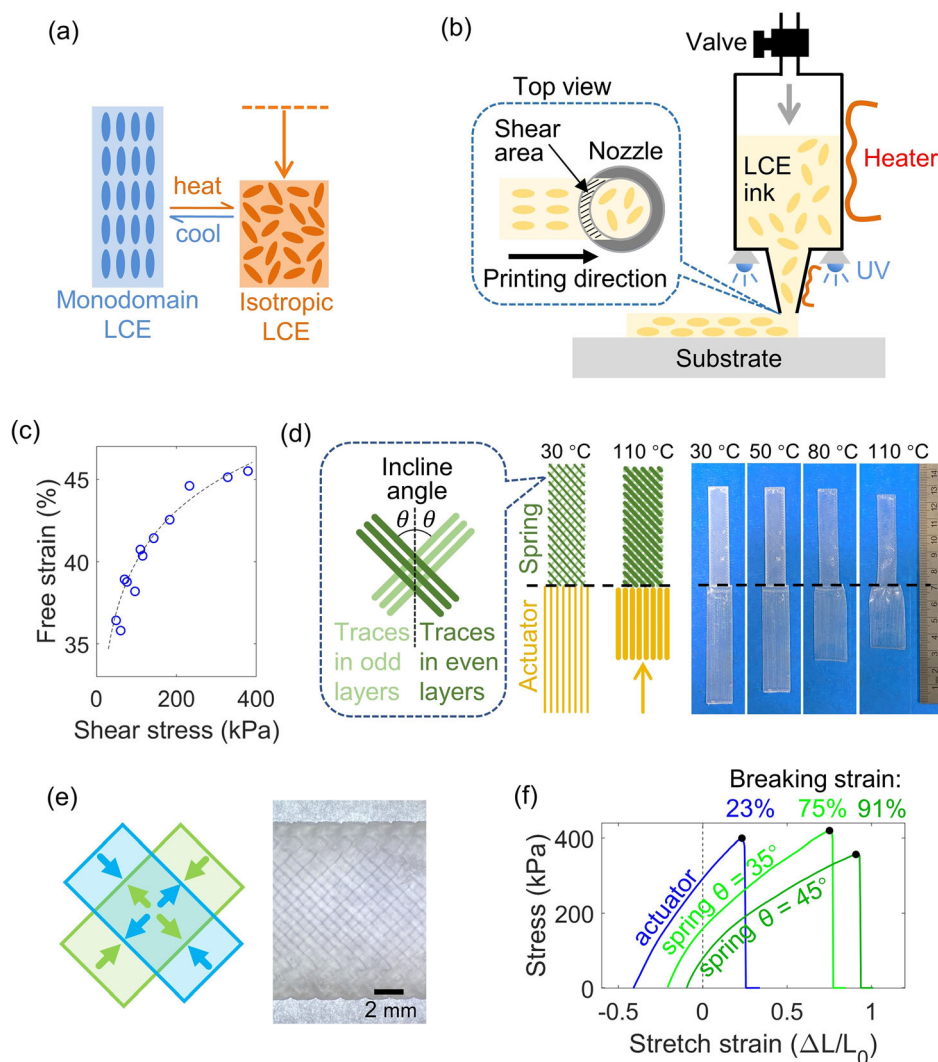
ADVANCED
SCIENCE NEWS
www.advancedsciencenews.com

ADVANCED
INTELLIGENT
SYSTEMS
Open Access
www.advintellsyst.com

Figure 1. a) Thermal actuation mechanism of the LCE. b) Extrusion printing to align LCE mesogens. The inset shows the area where the nozzle applied shearing force to the extruding LCE. c) Free strain of LCE actuators when heated from 30 to 130 °C, as a function of shear stress at the nozzle. d) Schematics of the printed LCE spring and actuator segments. The photographs contrast the dimensional changes at different temperatures, in which the spring showed minimal strain, whereas the actuator contracted to 45% strain. e) Photograph of the LCE spring metastructure, and a diagram of force vectors to explain how contraction and extension were canceled out. f) Stress–strain measurements taken at 100 °C, comparing the actuator versus springs with different infill angles. The strain of 0% corresponds to the original length at room temperature. The direction of stretch was applied along the long edge of each sample.

2.2. Mechanisms to Enable Self-Sustained Locomotion

In this work, the goal was to demonstrate a self-oscillatory design that generates continual locomotion under infrared light. **Figure 2**a shows the robot structure consisting of a soft LCE actuator+spring (artificial muscle) and hard polycarbonate components (exoskeleton). The key dimensions of the robot are listed in Table S1, Supporting Information. There were three hard components: a leg box, a body box, and a flipping shade fixed at the center of the leg box through a hinge. The shade was intended to rotate between the work and return stroke so that it would switch shading for either the spring or the actuator. At the four corners of the leg box, there were four protruding

cylindrical sliding bars, drawn as a circle attached to the leg in Figure 2b. The sliding bars on the leg box were inserted into the parallelogram tracks in the body box. Therefore, the leg box was constrained to slide around the parallelogram. The LCE actuator+spring connected the leg box to the body box. The contractive force from either the actuator or the spring would drive the relative movement between the leg box and body box.

A flow chart of the movement cycle is shown in Figure 2b, which zooms in on the operation at one of the four identical parallelogram tracks. Step (i) shows the standby state of the robot, in which there was minimal tension in both the actuator and the spring. The shade hovered over the spring segment, and the actuator was uncovered. If light was shone on the entire robot, the
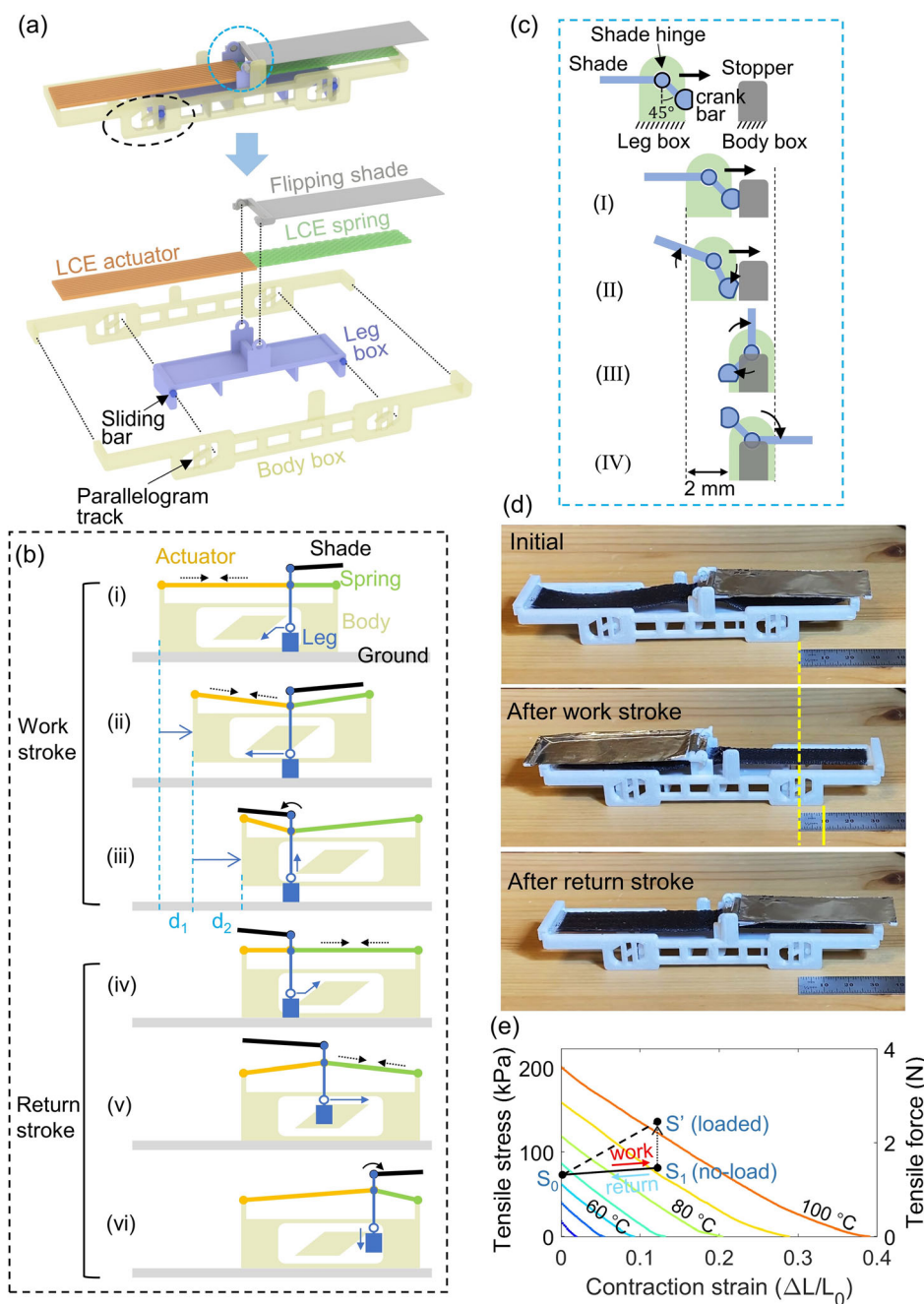
Figure 2. a) Assembly schematics and an exploded view of the printed robot. The black circle marks one of the four identical movement tracks, and the blue circle indicates the two shade hinges. b) Flow chart of the steps in one motion cycle. c) Flow chart of the shade flipping mechanism. d) Photographs of one motion cycle. e) Output stress–strain characteristics of the LCE actuator at different temperatures, in steps of 10 °C. The initial and actuated states of the actuator are marked as S_0 and S_1, respectively. When the robot carried a load, the actuated state changed to S'.

robot would proceed to step (ii), in which the actuator absorbed heat, consequently contracting and pulling to lift the body box from the ground and concurrently move the body horizontally. Between steps (i) and (ii), the horizontal moving distance of the body box was d_1, defined by the parallelogram dimensions. The exposed actuator kept absorbing light energy and contracted further, pulling the sliding bar across the bottom edge of the

parallelogram track. Between steps (ii) and (iii), the body box was translated farther to the right by a distance d_2. The shade flipping mechanism was triggered by the movement sequence and automatically turned the shade to cover the actuator. In step (iii), the body box would drop down to contact the ground again, because the sliding bar has moved to the top edge of the parallelogram track. Steps (i) to (iii) constitute the work stroke, in

**ADVANCED
SCIENCE NEWS**
www.advancedsciencenews.com

**ADVANCED
INTELLIGENT
SYSTEMS**
Open Access

www.advintellsyst.com

which the actuator converted the absorbed heat to mechanical energy to move the body box. Meanwhile, a portion of mechanical energy is stored in the stretched spring.

Following the work stroke, steps (iv) to (vi) were carried out to complete the return stroke. The movement around the parallelogram track is similar to a ratchet. As the shaded actuator cooled down, the tension in the stretched spring pulled on the actuator to return it to its initial length. Under the spring force, the sliding bar of the leg box is guided to move right and up the parallelogram track, and the leg box is lifted above the ground in step (iv). In step (v), the sliding bar traveled across the top edge of the parallelogram, and the leg box moved to the right as driven by the spring. The shade automatically switched to cover the spring. In step (vi), the sliding bar moved to the position where it was no longer supported by the parallelogram ledge, and the leg box dropped down onto the ground by gravity. At this moment, the robot finished one whole movement cycle and would be ready for another cycle. The total locomotion distance in one cycle was $d_1 + d_2$, traveled during the work stroke.

At the end of steps (ii) and (v), the shade should automatically flip to the opposite side to modulate the heating and cooling of the LCE so that despite constant irradiation there would be oscillating actuations to transition between strokes and enable self-sustained, unsupervised movement cycles. We implemented hinges that switched the shade position according to the relative movement between the body and leg boxes, as detailed in Figure 2c. The shade hinge was attached to the center of the leg box, and there were two crank bars, one on each side of the shade. In the schematic only one side was shown, but the other side worked in a similar fashion to flip the shade in the opposite direction. The crank bar was trimmed to have a flat edge, and its position was dictated by the leg box. The crank bar would work in conjunction with the rectangular stopper attached to the body box. As the leg box carried the crank bar toward the stopper, the two structures came into contact, but the interface friction stopped movement (step I). Then, the LCE contraction continued and built up elastic energy, which eventually exceeded the threshold to overcome friction and pushed the shade and crank bar to rotate (step II). As the friction on the arc of the crank bar was much smaller than on the flat edge, the stored elastic energy was released instantaneously, inducing an impulse force to rapidly erect the shade arm (step III). Following through due to its own rotary inertia and gravity, the shade would complete the 180° rotation, as shown in step IV. A slow-motion video showing the shade-flipping process is included in Supplemental Movie SM2.

The photographs in Figure 2d captured the robot locomotion in one movement cycle. Under a broadband light at an intensity of around $220\,mW\,cm^{-2}$, the robot moved about 10 mm during the work stroke, and the shade was flipped from the spring side to cover the actuator. For the 10 mm travel distance, the robot step was 8.6 mm, while an additional 1.4 mm slide was observed due to the forward launching momentum. During the return stroke, although the body box did not move, the leg box returned to the original position with respect to the body box, and the shade turned back to the spring side. A video showing ten successive cycles of self-sustained movement can be found in Supplemental Movie SM1.

Figure 2e shows the stress–strain characteristics of the LCE actuator at different temperatures. The measurements were taken in the active output region of the actuator, thus showing only contraction strain. The blocked stress is 200 kPa at 100 °C, and the blocked force of this actuator is 3.6 N. In a movement cycle, the starting state was marked as S_0, corresponding to 65 °C temperature and 0% strain. At the end of a work stroke, the actuator was fully actuated, marked as state S_1 in the plot, corresponding to 90 °C and 12.6% strain, as recorded by infrared camera and length measurements. The state of the actuator transitioned between S_0 and S_1, and the temperature changed between 65 and 90 °C. In the return stroke, the actuator under the shade did not need to be cooled to room temperature. When the robot is loaded with cargo, the actuator force output must increase to lift and translate the extra payload. As a result, the actuated state shifts upward to state S', in which the strain is still 12.6%, but the required actuation temperature and stress are increased.

2.3. Slope-Climbing Test

Our robot exhibited high traction force due to the high output stress of the LCE, and the LCE–exoskeleton combination offered unique capabilities for climbing steep slopes and carrying heavy payloads. **Figure 3**a shows our robot climbing up a slope of 40°, and a video is included as Supplemental Movie SM3. After ten successive cycles, the robot moved a distance of 70 mm, with an average step of 7 mm. This distance was shorter than the stepping distance on a flat surface, because instead of dropping straight down, the body box fell slightly backward due to the pitch angle during step (iii) of the movement cycle in Figure 2b. In the example in Figure 3a, the surface of the slope was coated with polydimethylsiloxane (PDMS) to prevent sliding. Nonetheless, similar climbing performance can be achieved by putting sandpaper or PDMS on the bottom surface of the robot to increase the contact friction with the ground. We observed that 40° was the maximum angle that the robot could climb. For the current design, the shade rotation mechanism worked against gravity and was stuck at step (v) when the pitch angle was higher than 40°. This limit of 40° slope corresponds to a percentage grade of 83.9%. As a comparison, most common wheeled vehicles are not able to climb a slope of this grade, and the steepest paved roads are below 20°.

2.4. Sunlight-Powered Locomotion

As our robot harvested infrared radiation to power the actuation cycles, we aimed to make it move with energy input only from natural sunlight, so to demonstrate the feasibility of running the robot autonomously for outdoor transportation. For indoor environments, high light power could be directed over the robot's track, but for the outdoors, our local sunlight irradiance was measured as only $\approx45\,mW\,cm^{-2}$ on the ground level and not powerful enough to drive the robot. Therefore, we attached a set of solar reflectors on the robot to concentrate more light on the LCE region, as shown in the Figure 3b inset. The reflector set was designed for a solar elevation angle of 35° and concentrated the sunlight power shone on the LCE area by seven times,
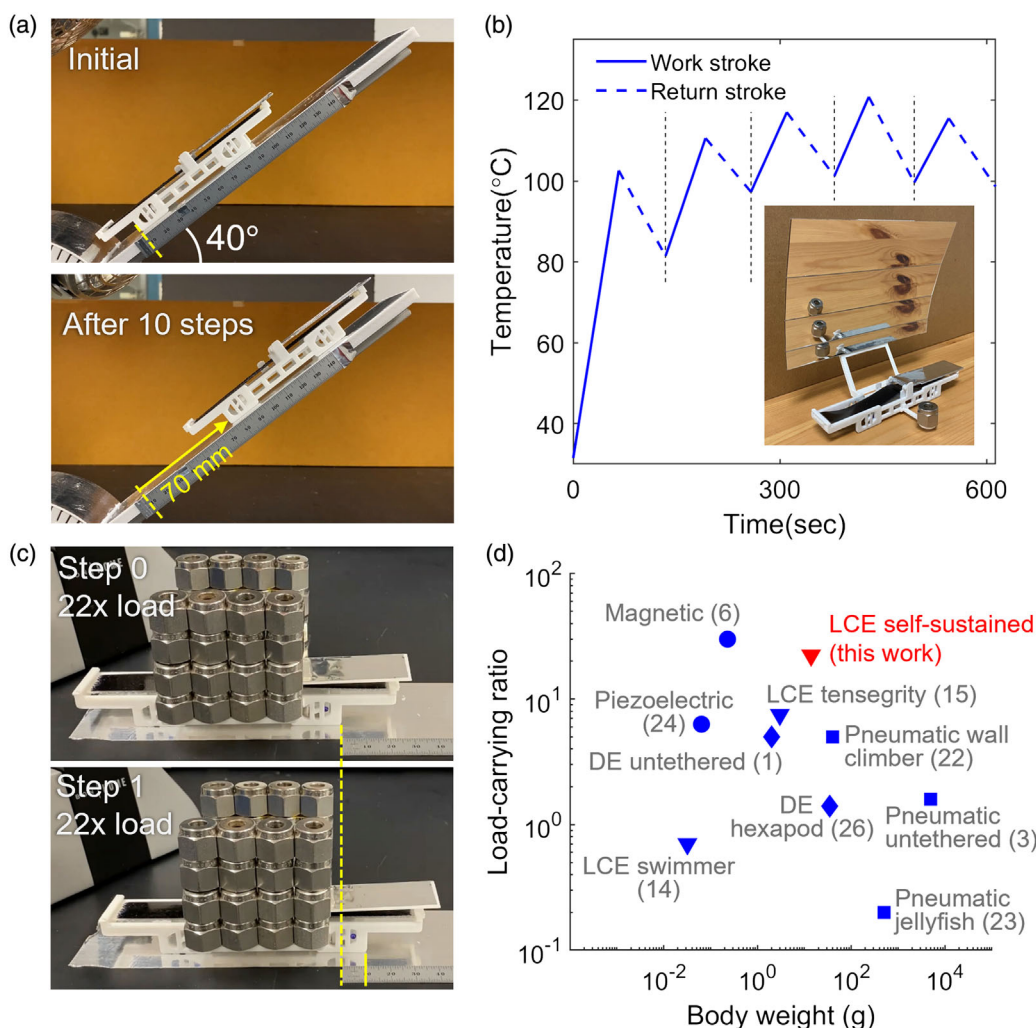
Figure 3. a) Demonstration of our robot climbing up a 40° slope. b) Temperature changes of the actuator segment over five successive movement cycles. The inset photograph shows the reflector attachment to concentrate ambient light toward the LCE. c) Robot transporting a load 22 times its body weight. d) Comparison of load-carrying ratio versus body weight for various robot designs based on soft actuators. DE: dielectric elastomer. The numbers correspond to the listings in the reference section.

leading to an irradiance ≈315 mW cm^{-2} on the robot. The schematic of the reflector is shown in Figure S3, Supporting Information, and a video of the robot locomotion under sunlight is attached as Supplemental Movie SM4.

With an infrared camera, the temperature of the LCE actuator was measured at the start and end time points of every stroke, as plotted in Figure 3b taken under an irradiance of 330 mW cm^{-2}. Starting at room temperature in the first cycle, the actuator temperature increased to 100 °C when the work stroke was completed. Then it dropped to 80 °C in the return stroke under the shade. The cycles of heating and cooling continued automatically by the shade-switching mechanism; from the third movement cycle onward, the operating temperatures were between 100 and 120 °C. The time duration for one cycle was stabilized to 116 s on average. The moving speed of the robot was dependent on the light intensity. As a comparison to measurements in Figure 2e under an input power of 220 mW cm^{-2}, the time for

one cycle was 161 s on average, and the temperature changed in the range of 65–90 °C. Higher irradiance could power the robot to work at a faster speed, but it also increased the operational temperatures. Because the LCE actuator tended to break due to high blocked stress when the temperature was above 120 °C, we limited the light irradiance to below 330 mW cm^{-2} to keep the operational temperature below the LCE breaking point. As shown in Figure S2c, Supporting Information, the nematic–isotropic phase transition temperature (T_{NI}) of the LCE was 83.0 °C, at which the phase transition was the largest and the free strain over temperature change was the highest. Without a load, the lowest operation temperature range of the robot was 65–90 °C, which included the T_{NI}. When the operation temperature range was higher, such as between 100 and 120 °C, the excess energy over T_{NI} resulted in larger contraction stress in the LCE components under the same strain, which can be used to drive a heavier load or to accelerate the robot motion.

**ADVANCED
SCIENCE NEWS**

www.advancedsciencenews.com

**ADVANCED
INTELLIGENT
SYSTEMS**
Open Access

www.advintellsyst.com

2.5. Load-Carrying Test

The robot is already shown to be capable of carrying the solar reflector (32 g), and we further characterized its load-carrying capacity in Figure 3c and Supplemental Movie SM5. The robot was able to transport a maximum mass of 311.7 g, whereas its body mass was 13.95 g, which accounted for the entire structure of the LCE (2.51 g) and the exoskeleton (11.44 g). The load-carrying ratio was 22.3 times. Under the maximum load, it traveled 10 mm per movement cycle. The load-carrying ratios of various robot designs based on soft actuators are displayed in Figure 3d. The comparison included driving mechanisms using the LCE,[14,15] dielectric elastomers,[1,26] magnetic elastomers,[6] piezoelectric polymers,[24] and pneumatically powered polymeric structures.[3,22,23] Here, our LCE self-sustained robot showed higher load-carrying capacity than the other robots with similar body weights, demonstrating the potential of hybrid LCE–exoskeleton structures in overcoming prior load limits of LCE robots.

2.6. Insect-Inspired Modification to Amplify the Step Length

With the aforementioned design, the robot stepping distance was just 6% of its body length (or 12.6% of the actuator length) in each movement cycle. This travel distance was constrained by the length of the parallelogram track; if the track was made longer with respect to the actuator length, the LCE contraction was insufficient to complete a stroke, and the robot was stuck. However, the LCE actuator had shown high work output to lift and transport very heavy loads compared to its body weight, indicating that there was a large portion of the actuation energy not spent on horizontal locomotion in this design. Therefore, there was room to channel more of the actuation output toward increasing the horizontal travel distance. We redirected part of the actuation energy to drive a lever mechanism that extended the stepping distance, so the robot could travel farther in each movement cycle while carrying less load.

Inspired by insects that use long legs to move their light and small bodies, we designed an attachment with four lever legs to fit onto the robot for extending its step length. The schematics and photograph of the attachment structure are shown in **Figure 4**a,b, respectively. The four lever legs were connected to the robot leg box through hinges and extended out through slots in the attachment body box, with its ledges serving as fulcrums of the lever legs. In the work stroke, as the actuator pulled the leg box toward the body box, the actuation motion simultaneously lifted up the robot body and propelled it forward, similar to the motion in step (i) shown in Figure 2b. Here the endpoints of the lever legs provided the four contact points to the ground, as shown in Figure 4a. In the return stoke, the robot rested on the attachment box, and then the lever legs were lifted to return to a starting position, ready for a new cycle. This return motion avoided dragging the body backward.

For each lever leg, the length ratio of the segments on the two sides of the fulcrum was 1:8.2, with the short segment inside and the long segment outside the body box. By lever action, a displacement of the short segment would result in an amplified displacement of the long segment proportional to the length-ratio factor. Therefore, the small 8.6 mm step in the original robot design was amplified by 8.2 times by the lever legs, for the modified robot to traverse 70 mm per step. Figure 4c shows the locomotion of the modified robot, carrying a load equal to its body mass while advancing roughly a quarter of its body length per minute, as recorded in Supplemental Movie SM6.

3. Discussion

This work demonstrated three new concepts for LCE actuation: 1) the design of a self-sustained oscillation mechanism to store and release energy from a constant input; 2) the decoupling of mechanical properties from thermal response by tuning print toolpaths to fabricate novel, highly elastic spring components for energy storage; and 3) the use of exoskeleton structures to increase load-carrying capacity or stepping distance. The improvements in printing toolpaths enabled freeform tuning of the LCE characteristics; the printing process realized a state-of-the-art actuator, reaching a maximum free strain of 45.5% and a blocked stress of 200 kPa at 100 °C. By adapting the toolpaths, the same LCE material was fabricated into a highly elastic spring with a breaking strain of 91%.

In the robot design, the exoskeleton enables both self-oscillating movements and load-supporting functions. Our robot operation did not require external signaling controls or complex electronics. Under a constant light input, the robot achieved self-sustained cycles like a heat engine, absorbing heat from light energy to do work. The features of self-sustained locomotion and high load-carrying capability show the potential for this robot design to be used for transportation in unsupervised environments. To include a steering function in future designs, we may combine two robot units side by side with linkages. When driving the robot, if light is shined on both units, the light could drive it forward in a straight path. If the light only shines on one of the units, because of the asynchronous motion, the robot could be steered to one side. The robot is scalable in size and can be modified to increase the load capacity or moving speed by using peripheral structures such as the lever legs.

To enable repetitive oscillations, our robot used an energy storage spring to restore the actuator position after contraction, and the crank design allowed the generation of impulse energy for rapid rotation of the flipping shade. The straight chord on the hinge crank bar served as a frictional barrier to build up tension stress and store more energy before the rotation mechanism was triggered. When the activation threshold was overcome by the tension, the impulse energy released led to rapid complete rotation, so the work stroke would not be stuck when the shade is in a midway perpendicular state.

One key aspect of our robot was that the two-phase contraction and extension of the LCE actuator were expanded into a six-phase movement cycle through the incorporation of parallelogram tracks. The track divided the cyclic movements of the sliding bar into two different paths in the work and return strokes, so the locomotion was unidirectional. Such cyclic designs are commonly found in retractable pens and self-lock buttons, in which the sequential pressing and releasing of a button moves in divided paths. Although such structures ensured automated cycles, part of the energy was traded off between lifting movement and forward movement of our robot.

In a movement cycle, the work of the LCE actuator was consumed in two parts, by 1) the frictional heat between components and 2) the gravitational potential energy of lifting the body or leg
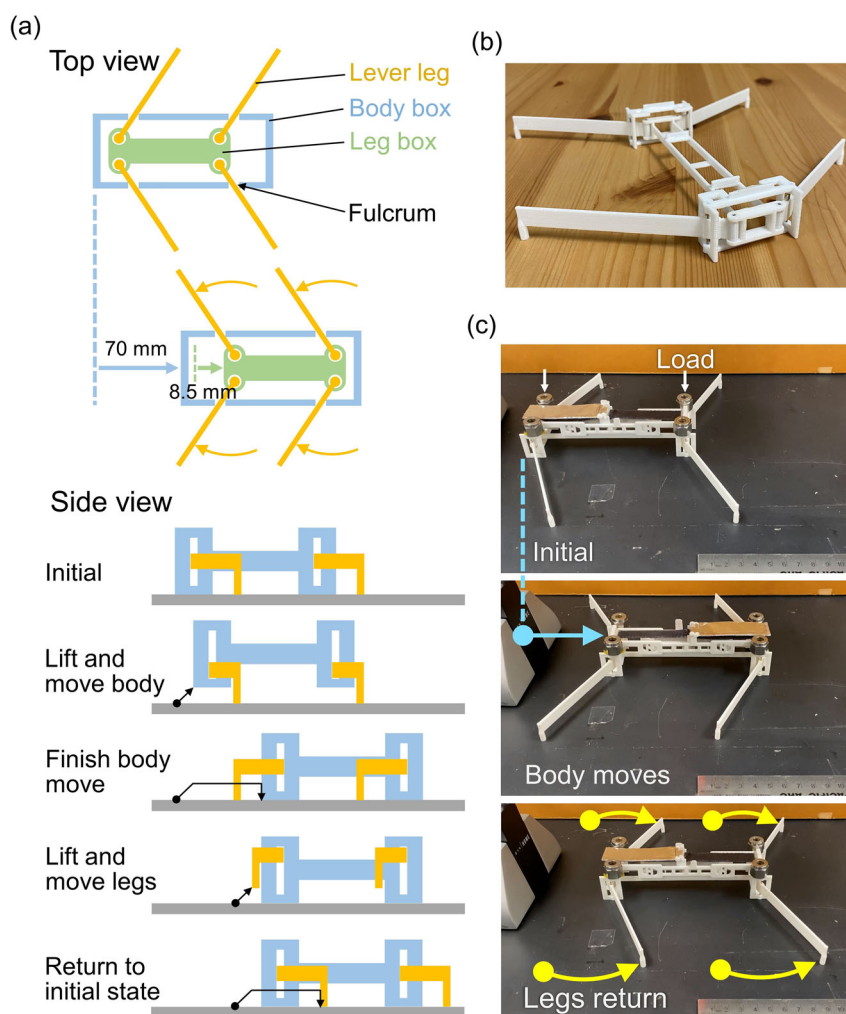
**ADVANCED
SCIENCE NEWS**
www.advancedsciencenews.com

**ADVANCED
INTELLIGENT
SYSTEMS**
Open Access
www.advintellsyst.com

Figure 4. a) Schematics of the robot equipped with lever legs to amplify the stepping distance. Top view and side view. b) Photograph of the lever attachment. c) Photograph of the movement sequence.

box. Especially when the robot was heavily loaded, a large amount of potential energy was required to lift the body box. This component of energy was consumed in up-and-down displacement and not used for forward movement. Therefore, reducing the lift distance would be a design consideration to reduce unnecessary energy consumption and increase the load-carrying ability. The lift distance Δh was determined from $\Delta h = (H + D)/2$, where in our demonstration, $H = 3$ mm was the height of the parallelogram stub, $D = 2.5$ mm was the diameter of the sliding bar, and therefore $\Delta h = 2.75$ mm was the lift distance in each cycle. To reduce the energy spent on lift movement, both H and D should be reduced. However, in the current proof-of-concept design, the feature size was limited by the resolution of fused deposition modeling (FDM) printing; also the strength of smaller stubs for the parallelogram and sliding bar was not enough to support heavy loads. Therefore, to advance performance in the future, other high-precision printing methods such as stereolithography and high-strength materials for the exoskeleton can be used to scale down robots and enable very high load-carrying ratios.

In addition, it is possible to increase the robot speed. Currently the locomotion speed is limited by the heat absorption and dissipation time. As the heating and cooling processes are both related to surface areas, one design strategy is to reduce the total thickness of the LCE layers while increasing their widths. As this change will maintain the same cross-sectional area, the robot will keep the same load-carrying ability. With the same heat capacity but a larger surface area, the heat transfer will be faster and the robot movement will be accelerated. Overall, the bioinspired robot in this work offers new elements of self-oscillation and structural modifications to amplify load and step size, and the strategies can be generally applicable to future locomotion robot designs.

4. Experimental Section

Preparation of LCE Ink: The LCE extrusion ink was synthesized from monomer 1,4-bis-[4-(3-acryloyloxypropyloxy) benzoyloxy]-2-methylbenzene (RM257, 98.8%, Wilshire technologies) and 2,2′-(ethylenedioxy) diethanethiol (EDDET, 95%, Sigma-Aldrich). Aiming for an ink with the degree of

polymerization equal to 8, 0.04 mole of RM257 and 0.035 mole of EDDET were dissolved in 80 mL dichloromethane. Then 0.54 mL dipropylamine was added into the solution as the polymerization catalyst. The solution was stirred for 24 h at room temperature. Subsequently, 0.11 g 2-hydroxy-4′-(2-hydroxyethoxy)-2-methylpropiophenone was added to the solution as a photoinitiator. Then in a round bottom flask the solution was stirred and heated to 70 °C on a heating mantle (Mtops DMS632) to evaporate the solvent. In 1 h, most of the solvent was removed, and then the flask was connected to a vacuum and heated to 90 °C for 23 h to remove the residual solvent and catalyst. During heating, the flask was covered by aluminum foils to avoid crosslinking induced by florescent lights in the room. After solvent evaporation, the LCE ink was loaded into a 10 mL dispensing syringe. A hot air gun set to 240 °C was used to heat the flask to reduce the ink viscosity for it to flow out. Then the dispensing syringe was held vertically and heated in an oven to 80 °C for 24–48 h for the ink to settle and degas.

Printing Setup: A schematic of our printer is shown in Figure 1a. It was modified from a Raise3D N2 platform, with the option to use a FDM nozzle and a pneumatic extrusion nozzle with compressed air supply in the range of 0–90 psi. The air supply was controlled by a dispenser with a pressure regulator and a solenoid valve. The LCE ink was stored in a dispensing syringe and extruded through an 18-gauge needle nozzle. There were heaters for the syringe and the nozzle to increase the temperature of the LCE ink, to reduce the ink viscosity for smooth extrusion.[33,41] During printing, a load cell (SEN-14 728, 0.5 kgf, Digi-Key) with the HX-711 ADC module was used to track the shear force. There were UV light emitting diodes mounted next to the nozzle for cross-linking the workpiece.

Stress–Strain Characterization: An S-type load cell (DY106-3 kg) was attached on a 3D printer frame (prusa i3) to modify it into a programmable tensile force tester. A pair of metal fixtures was used in the tester to hold the samples. The analog feedback value from the load cell was sampled by a HX-711 AD convertor, and the data were read by an Arduino chip. A MATLAB program was used to control the movement of the tester and record the force value from Arduino.

The LCE actuator or spring was clamped between the top and bottom fixtures. A 205 W infrared heat lamp (Bon Home Culinary Heat Lamp) was used to heat the sample. The distance between the lamp and sample was tuned to adjust the temperature, which was tracked by a thermal imager (PerfectPrime IR0005). In the measurements, the sample was fixed at the original length. Then the temperature of the sample was controlled to the desired temperatures between 40 and 100 °C. When the temperature was stabilized, the readout force was the blocking force. Then the printer frame was controlled to allow the sample length to change, and meanwhile the contraction force was recorded at each length. When the contraction force was reduced to zero, the sample reached the maximum free strain at a specific temperature, and one measurement cycle was completed. The sample was stretched by the frame to its original length and was heated to another temperature, repeating the measurement process.

Fabrication of the Robot: The dimensions of robot components are listed in Table S1, Supporting Information. The body box, leg box, and frame of the flipping shade were printed with 1.75 mm polycarbonate filament (PC-Max) in the FDM mode. The layer thickness was set to 0.2 mm, and the global printing speed was 15 mm s^{-1}. The nozzle temperature was 270–285 °C, and the platform was heated to 110 °C. "Bottom raft" and "support everywhere" settings were used to increase the yield. To avoid wrapping of the polycarbonate, the printer was enclosed to minimize air flow. The cooling fans were disabled, and aluminum foils were wrapped around the nozzle to prevent any air blown toward the printed workpiece. After printing, the raft and support structures were removed by pliers. Then the surface was polished by precision files, 320-grit sand paper, and 1000-grit sand paper. Aluminum foils were mounted for the flipping shade to block infrared radiation.

The LCE actuator and spring were printed at 90 psi, with the syringe at 55 °C, the nozzle at 60 °C, and a flow rate of 0.5 mm^3 s^{-1}. In each printing pass, the layer thickness was 0.1 mm, and there were 12 layers in total. The area of the actuator was 68 × 15 mm^2, and the spring was 60 × 12 mm^2 with traces printed at 35° incline angle. The actuator and spring were printed and connected in one piece, but the toolpaths were different in each segment. A 200 mW UV light was used to cross-link the LCE during printing. After printing, the sample was cured by 10 W UV light for 5 min to fully cross-link. The surface of LCE components was painted black with a marker pen to increase light absorption.

The polycarbonate exoskeleton components were assembled with the LCE actuator+spring into one structure. Using instant adhesive (Loctite 495), the middle of the LCE piece was glued to the center point on the leg box, while the ends of the LCE structure were glued to the ends of the body box.

Light Source for Powering the Robot: A 205 W infrared heat lamp (Bon Home Culinary Heat Lamp) was used as light source. The black-body temperature was 530 °C, leading to a peak wavelength of ≈3.6 μm. The distance between the lamp and the robot was tuned in the range of 8–13 cm to achieve a light power of 220–330 mW cm^{-2}. The light power was measured on a piece of brass that was painted black, and the increase of temperature was tracked with a thermal imaging camera (PerfectPrime IR0005). When testing the robot, the temperature of the LCE was also measured by the thermal imaging camera.

Slope-Climbing Test: In the slope-climbing test, an adjustable ramp was printed with a polycarbonate by FDM. The top surface was covered with a plastic mirror sheet to avoid overheating the plastic pad. The surface of the mirror was coated with PDMS (Sylgard 184) to increase traction with the robot. During testing, the slope angle was increased by 5° increments to find the limit when the robot could not complete a whole movement cycle.

Load-Carrying Test: Two cargo support plates were printed with polycarbonate and attached to the two sides of the robot with instant adhesive. Metal nuts were added on the cargo plates as loads. The weight of each nut was 9.7 g.

Sunlight Reflector Attachment: The supporting frame of the reflectors was printed with polylactic acid filaments by FDM. Plastic mirrors were attached on the frame with instant adhesive. The frame and a balancing weight were attached on two sides of the robot. The demonstration of robot locomotion powered by sunlight was conducted at noon, and the solar elevation angle was about 35°.

Lever Leg Attachment: The long lever legs and corresponding supporting components were printed with polycarbonate and attached onto the robot with instant adhesive. The rotation hinges of the legs were connected by 18-gauge rods. The mechanism of the lever legs is shown in more detail in the Figure S4–S10 and Movie SM7, Supporting Information.

Supporting Information

Supporting Information is available from the Wiley Online Library or from the author.

Acknowledgements

Conflict of Interest

The authors declare no conflict of interest.

Data Availability Statement

The data that support the findings of this study are available from the corresponding author upon reasonable request.

**ADVANCED
SCIENCE NEWS**

www.advancedsciencenews.com

**ADVANCED
INTELLIGENT
SYSTEMS**

www.advintellsyst.com

[1] X. Ji, X. Liu, V. Cacucciolo, M. Imboden, Y. Civet, A. El Haitami, S. Cantin, Y. Perriard, H. Shea, *Sci. Rob.* **2019**, *4*, eaaz6451.

[2] Q. He, Z. Wang, Y. Wang, A. Minori, M. T. Tolley, S. Cai, *Sci. Adv.* **2019**, *5*, eaax5746.

[3] M. T. Tolley, R. F. Shepherd, B. Mosadegh, K. C. Galloway, M. Wehner, M. Karpelson, R. J. Wood, G. M. Whitesides, *Soft Rob.* **2014**, *1*, 213.

[4] T. Li, G. Li, Y. Liang, T. Cheng, J. Dai, X. Yang, B. Liu, Z. Zeng, Z. Huang, Y. Luo, T. Xie, W. Yang, *Sci. Adv.* **2017**, *3*, 1602045.

[5] H. Lee, Y. Jang, J. K. Choe, S. Lee, H. Song, J. P. Lee, N. Lone, J. Kim, *Sci. Rob.* **2020**, *5*, eaay9024.

[6] E. B. Joyee, A. Szmelter, D. Eddington, Y. Pan, *Soft Rob.* **2020**, http://doi.org/10.1089/soro.2020.0004.

[7] C. Li, G. C. Lau, H. Yuan, A. Aggarwal, V. L. Dominguez, S. Liu, H. Sai, L. C. Palmer, N. A. Sather, T. J. Pearson, D. E. Freedman, P. K. Amiri, M. O. de la Cruz, S. I. Stupp, *Sci. Rob.* **2020**, *5*, eabbb9822.

[8] X. Yang, W. Shang, H. Lu, Y. Liu, L. Yang, R. Tan, X. Wu, Y. Shen, *Sci. Rob.* **2020**, *5*, eabc8191.

[9] Y. Kim, H. Yuk, R. Zhao, S. A. Chester, X. Zhao, *Nature* **2018**, *558*, 274.

[10] X. Lu, S. Guo, X. Tong, H. Xia, Y. Zhao, *Adv. Mater.* **2017**, *29*, 1606467.

[11] H. Zeng, O. M. Wani, P. Wasylczyk, A. Priimagi, *Macromol. Rapid Commun.* **2018**, *39*, 1700224.

[12] M. Pilz da Cunha, M. G. Debije, A. P. H. J. Schenning, *Chem. Soc. Rev.* **2020**, *49*, 6568.

[13] H. Zeng, P. Wasylczyk, C. Parmeggiani, D. Martella, M. Burresi, D. S. Wiersma, *Adv. Mater.* **2015**, *27*, 3883.

[14] C. Huang, J. Lv, X. Tian, Y. Wang, Y. Yu, J. Liu, *Sci. Rep.* **2015**, *5*, 17414.

[15] Z. Wang, K. Li, Q. He, S. Cai, *Adv. Mater.* **2019**, *31*, 1806849.

[16] G. Cai, J.-H. Ciou, Y. Liu, Y. Jiang, P. S. Lee, *Sci. Adv.* **2019**, *5*, eaaw7956.

[17] B. Shin, J. Ha, M. Lee, K. Park, G. H. Park, T. H. Choi, K.-J. Cho, H.-Y. Kim, *Sci. Rob.* **2018**, *3*, eaar2629.

[18] Y. Zhao, C. Xuan, X. Qian, Y. Alsaid, M. Hua, L. Jin, X. He, *Sci. Rob.* **2019**, *4*, eaax7112.

[19] J. J. Wie, M. R. Shankar, T. J. White, *Nat. Commun.* **2016**, *7*, 13260.

[20] A. Kotikian, C. McMahan, E. C. Davidson, J. M. Muhammad, R. D. Weeks, C. Daraio, J. A. Lewis, *Sci. Rob.* **2019**, *4*, eaax7044.

[21] M. Wang, Z.-W. Cheng, B. Zuo, X.-M. Chen, S. Huang, H. Yang, *ACS Macro Lett.* **2020**, *9*, 860.

[22] Y. Tang, Q. Zhang, G. Lin, J. Yin, *Soft Rob.* **2018**, *5*, 592.

[23] A. Joshi, A. Kulkarni, Y. Tadesse, *Robotics* **2019**, *8*, 56.

[24] Y. Wu, J. K. Yim, J. Liang, Z. Shao, M. Qi, J. Zhong, Z. Luo, X. Yan, M. Zhang, X. Wang, R. S. Fearing, R. J. Full, L. Lin, *Sci. Rob.* **2019**, *4*, eaax1594.

[25] G. Gu, J. Zou, R. Zhao, X. Zhao, X. Zhu, *Sci. Rob.* **2018**, *3*, eaat2874.

[26] C. T. Nguyen, H. Phung, T. D. Nguyen, H. Jung, H. R. Choi, *Sens. Actuators, A* **2017**, *267*, 505.

[27] V. Nguyen, B. Lilly, C. Castro, *J. Biomech.* **2014**, *47*, 497.

[28] C. Wang, K. Sim, J. Chen, H. Kim, Z. Rao, Y. Li, W. Chen, J. Song, R. Verduzco, C. Yu, *Adv. Mater.* **2018**, *30*, 1706695.

[29] R. S. Kularatne, H. Kim, J. M. Boothby, T. H. Ware, *J. Polym. Sci., Part B: Polym. Phys.* **2017**, *55*, 395.

[30] S. W. Ula, N. A. Traugutt, R. H. Volpe, R. R. Patel, K. Yu, C. M. Yakacki, *Liq. Cryst. Rev.* **2018**, *6*, 78.

[31] A. Kotikian, R. L. Truby, J. W. Boley, T. J. White, J. A. Lewis, *Adv. Mater.* **2018**, *30*, 1706164.

[32] Z. Wang, Z. Wang, Y. Zheng, Q. He, Y. Wang, S. Cai, *Sci. Adv.* **2020**, *6*, eabc0034.

[33] Y. Zhai, Z. Wang, K. S. Kwon, S. Cai, D. Lipomi, T. N. Ng, *Adv. Mater.* **2020**, 2002541.

[34] M. Kaur, T.-H. Kim, W. S. Kim, *Adv. Mater.* **2021**, *33*, 2002534.

[35] Y. J. Tan, G. J. Susanto, H. P. Anwar Ali, B. C. K. Tee, *Adv. Mater.* **2020**, *33*, 2002800.

[36] K.-S. Kwon, T. N. Ng, *Org. Electron.* **2014**, *15*, 294.

[37] N. Li, N. Eedugurala, D.-S. Leem, J. D. Azoulay, T. N. Ng, *Adv. Funct. Mater.* **2021**, *31*, 2100565.

[38] S.-E. Wu, L. Yao, A. Shiller, A. H. Barnard, J. D. Azoulay, T. N. Ng, *Adv. Electron. Mater.* **2021**, *7*, 2100223.

[39] A. Vohra, K. Schlingman, R. S. Carmichael, T. B. Carmichael, *Chem* **2018**, *4*, 1673.

[40] Y. Zhai, J. Lee, Q. Hoang, D. Sievenpipper, H. Garudadri, T. N. Ng, *Flexible Printed Electron.* **2018**, *3*, 035006.

[41] Y. Bonnassieux, C. J. Brabec, Y. Cao, T. B. Carmichael, M. L. Chabinyc, K.-T. Cheng, G. Cho, A. Chung, C. L. Cobb, A. Distler, H.-J. Egelhaaf, G. Grau, X. Guo, G. Haghiashtiani, T.-C. Huang, M. M. Hussain, B. Iniguez, T.-M. Lee, L. Li, Y. Ma, D. Ma, M. C. McAlpine, T. N. Ng, R. Österbacka, S. N. Patel, J. Peng, H. Peng, J. Rivnay, L. Shao, D. Steingart, R. A. Street, V. Subramanian, L. Torsi, Y. Wu, *Flexible Printed Electron.* **2021**, *6*, 023001.